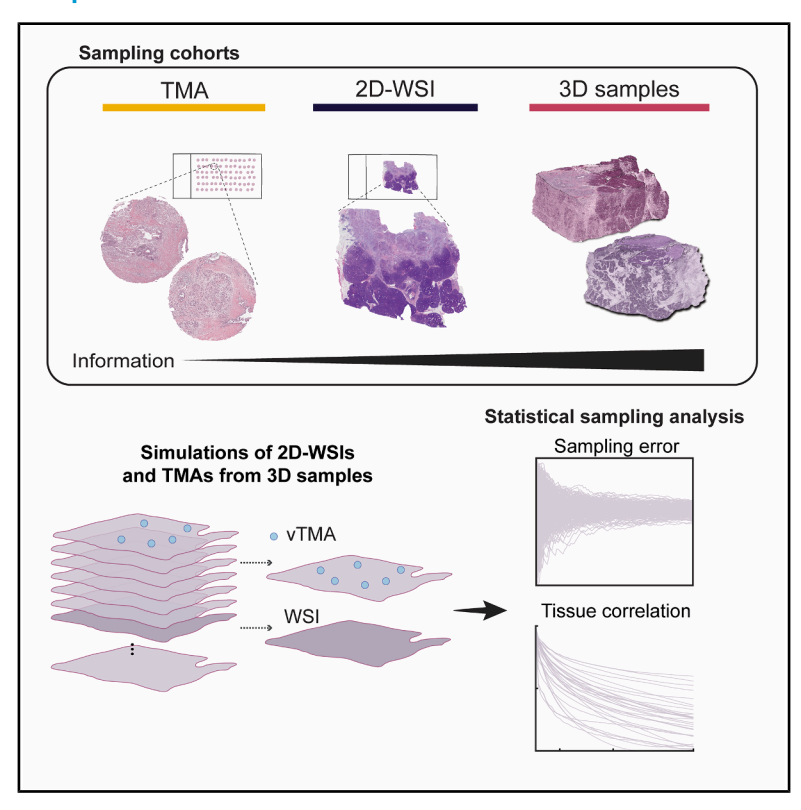
Three-dimensional assessments are necessary to determine the true, spatially resolved composition of tissues

Graphical abstract



Authors

André Forjaz, Eduarda Vaz, Valentina Matos Romero, ..., Laura D. Wood, Ashley L. Kiemen, Denis Wirtz

Correspondence

kiemen@jhmi.edu (A.L.K.), wirtz@jhu.edu (D.W.)

In brief

Forjaz et al. demonstrate that tissue structure and composition vary rapidly in three dimensions, revealing the limitations of traditional 2D pathology techniques. Their findings highlight the need for 3D imaging to accurately capture tissue heterogeneity and improve the assessment of both normal and disease microanatomical changes.

Highlights

- 3D imaging reveals tissue composition changes rapidly across microns of depth
- 2D assessments fail to capture tissue heterogeneity in normal and tumor tissue
- Biopsy cores quickly lose target features as serial sections are cut
- 3D imaging is needed for accurate profiling of tumor microenvironment



Resource

Three-dimensional assessments are necessary to determine the true, spatially resolved composition of tissues

André Forjaz,¹ Eduarda Vaz,¹ Valentina Matos Romero,¹ Saurabh Joshi,¹ Vasco Queiroga,¹ Alicia M. Braxton,² Ann C. Jiang,³ Kohei Fujikura,⁴ Toby Cornish,⁵ Seung-Mo Hong,⁶ Ralph H. Hruban,^{7,8} Pei-Hsun Wu,¹,९ Laura D. Wood,^{7,8,9} Ashley L. Kiemen,^{7,8,9,10,*} and Denis Wirtz¹,7,8,9,11,*

https://doi.org/10.1016/j.crmeth.2025.101075

MOTIVATION Spatially resolved cellular profiling methods are essential tools for studying tissue heterogeneity, yet they typically assess limited regions, requiring numerous samples to accurately capture tissue heterogeneity. Recent advances in three-dimensional (3D) tissue mapping offer deeper insights; however, attempts to quantify the information gained remain limited. Here, we comprehensively evaluate inter- and intra-sample heterogeneity using tissue cores, whole-slide images (WSIs), and 3D samples from over 100 pancreatic tissues. Our analysis quantifies the impact of sampling and defines sampling strategies to approximate the compositional heterogeneity observed in large-scale 3D tissues.

SUMMARY

Methods for spatially resolved cellular profiling of tissue sections enable in-depth study of inter- and intrasample heterogeneity but often profile small regions, requiring evaluation of many samples to compensate for limited assessment. Recent advances in three-dimensional (3D) tissue mapping offer deeper insights; however, attempts to quantify the information gained in transitioning to 3D remains limited. Here, to compare inter- and intra-sample tissue heterogeneity, we analyze >100 pancreas samples as cores, whole-slide images (WSIs), and cm³-sized 3D samples. We show that tens of WSIs and hundreds of tissue microarrays are needed to approximate the compositional tissue heterogeneity of tumors. Additionally, spatial correlations of pancreatic structures decay significantly within microns, demonstrating that isolated two-dimensional (2D) sections poorly represent their surroundings. Through 3D simulations, we determined the number of slides necessary to accurately measure tumor burden. These results quantify the power of 3D mapping and establish sampling methods for biological studies prioritizing composition or incidence.

INTRODUCTION

Recent developments in spatial profiling technologies have led to the construction of atlases to characterize cellular and tissue compositions, structure, and the "omic" (genomic, epigenomic, transcriptomic, proteomic, and metabolomic) landscapes of tissues, organs, and whole organisms. ^{1–9} These techniques have

led to important discoveries regarding changes in cellular composition during development, aging, and the progression of diseases such as cancer and cardiovascular disease. Due to technical and financial limitations, current spatial omic methods are designed to evaluate mm²-sized two-dimensional (2D) regions. ^{1,6,10-14} Recently, teams have developed novel techniques, such as open-top light-sheet, micro-computed tomography (micro-CT),

¹Department of Chemical & Biomolecular Engineering, Johns Hopkins University, Baltimore, MD, USA

²Department of Comparative Medicine, Medical University of South Carolina, Charleston, SC, USA

³Department of Biomedical Engineering, Johns Hopkins University, Baltimore, MD, USA

⁴Department of Medical Genetics, Life Sciences Institute, University of British Columbia, Vancouver, BC, Canada

⁵Department of Pathology, Data Science Institute, Medical College of Wisconsin, Milwaukee, WI 53226, USA

⁶Department of Pathology, Asan Medical Center, University of Ulsan College of Medicine, Seoul, Republic of Korea

⁷Department of Pathology, The Sol Goldman Pancreatic Cancer Research Center, Johns Hopkins School of Medicine, Baltimore, MD, USA

⁸Department of Oncology, Johns Hopkins School of Medicine, Baltimore, MD, USA

⁹The Johns Hopkins Institute for NanoBioTechnology, Johns Hopkins University, Baltimore, MD, USA

¹⁰Department of Functional Anatomy & Evolution, Johns Hopkins School of Medicine, Baltimore, MD, USA

¹¹Lead contact

^{*}Correspondence: kiemen@jhmi.edu (A.L.K.), wirtz@jhu.edu (D.W.)



serial-section-based imaging for three-dimensional (3D) tissue mapping. ^{15–18} However, attempts to quantify the amount of information gained in the transition from 2D to 3D have been limited. The purpose of this manuscript is to interrogate the added value of quantitative 3D pathology over classical 2D analysis. Here, to evaluate the loss in information when comparing inter- and intra-sample tissue heterogeneity, we analyze >100 pancreas tissue samples in the form of tissue cores, whole-slide images (WSIs), and cm³-sized 3D samples.

Consider a histological section of standard, 4 μ m thickness: a 1-mm² core of a tissue microarray (TMA) represents a volume of tissue of just 0.004 mm³, while a common region size for spatial transcriptomics (6.5 \times 6.5 mm²) corresponds to a volume of 0.2 mm³. These volumes represent minuscule fractions of the human organs that they are used to represent. More standard techniques, including WSIs stained with hematoxylin and eosin (H&E) or immunohistochemistry (IHC), are often considered the gold standard of diagnostic anatomic pathology. These slides feature a lateral area of 2 \times 5 cm², corresponding to a volume of 5 mm³. The implicit assumption of 2D sampling is that the cells within the sampled region, as well as their morphologies, densities, and cellular and non-cellular neighborhoods, are representative of those of the 3D organs and diseased tissues from which they are obtained.

Accurate clinical diagnosis of a range of diseases using single 2D H&E sections (selectively chosen from gross inspection of resected tissues) shows that the generalization of findings from 2D is possible, although recent works suggest that relevant criteria, including cancer grade and cancer precursor type, may be easily misdiagnosed in 2D. ^{16,21–24} In research settings, where the goal of tissue atlas efforts is generalizability, we hypothesize that 2D sampling may be insufficient to capture the marked intra-sample heterogeneity in cellular composition and tissue architecture.

Recent 3D work has demonstrated the utility of tissue clearing and serial-sectioning-based approaches to assess microanatomical maps of large (>1 cm³) volumes of tissue at cellular resolution. 16,17,25-37 Here, we use the recently developed 3D imaging workflow CODA to assess the spatial composition of key cell types in thick slabs of both grossly normal human pancreas tissue and human pancreas tissue containing pancreatic ductal adenocarcinoma (PDAC), the deadliest form of pancreatic cancer. 17 CODA was recently advanced to enable user interfaceguided workflows in an open-source programming language³⁸ and has been used to quantitatively interrogate normal human organ development, as well as breast cancer, prostate cancer, pancreatic cancer, diabetic neuropathy, myocarditis, skin regeneration, and fetal development in murine and human tissues. 28,39-47 The uniquely heterogeneous spatial microenvironment of PDAC makes it an optimal testbed to evaluate the benefits of 3D microanatomic mapping over standard 2D approaches.48-50

Our exhaustive analysis demonstrates that standard 2D sampling—using a limited number of TMA cores or WSIs—is typically insufficient for accurate assessment of tissue composition or tumor content or the selection of regions of interest (ROIs) for the creation of TMA cores and capturing rare events. ⁴³ We determine that tens of WSIs and hundreds of TMA cores are necessary to accurately represent the range of tissue compositions

present in a cm³-sized human pancreas sample. We find that sections inside a tumor, sometimes just tens of microns apart, can have completely different, uncorrelated cellular and noncellular structures. 2D assessments of "representative" slides fail particularly in the enumeration of rare events, such as the estimation of the density of cancer or cancer precursor cells in samples known to have low neoplastic content. ^{27,43} This work helps clarify the impact of tissue subsampling in the study of the composition of normal and malignant tissues, using analysis of 2D and 3D pancreatic human tissue samples as a testbed.

RESULTS

Construction of cohorts of 2D and 3D microanatomically labeled pancreatic tissue

To interrogate the differences between inter-sample and intrasample compositional heterogeneity, pancreatic tissue from 149 individuals was retrospectively collected, consisting of 101 samples containing invasive pancreatic cancer and 48 samples containing grossly normal pancreas (Figure 1A). Three cohorts consist of (1) the "2D-WSI" cohort, which has 64 individual, pathologist-curated WSIs; the "3D-CODA" cohort, which has 14 samples containing serially sectioned 3D blocks (seven of which contain invasive pancreatic cancer); and the "TMA" cohort, which is a single TMA containing pancreas histology from 30 individuals. Cohorts were matched between the TMA, WSI, and 3D cohorts according to age and gender (Table S1).

We used a segmentation algorithm to label microanatomical components to a resolution of 1 μ m (see STAR Methods). Independent testing showed an overall accuracy of 93.2% across all samples (Figure S1). For the 3D-CODA cohort, image registration was performed to create digital tissue volumes (Figure 1B). The minimum number of sections for these 3D samples was 270 (mean: 297, interquartile range: 816). The median reconstructed volume was 39.0 mm³ (mean: 132.2 mm³, interquartile range: 247.3 mm³). Statistical sampling was conducted on the 2D and 3D cohorts to evaluate the impact of sampling on tissue composition analysis of heterogeneous microanatomical tissue components (Figure 1C).

Spatial correlation rapidly decays within pancreatic tumors

To assess the structural continuity of tissues, we calculated how rapidly tissue composition changed along a straight line through the 3D tumors. To determine the correlation length of each tissue component (PDAC, vasculature, fat, ducts, etc.)—i.e., the distance over which the composition remained significantly correlated—we calculated the pixel-to-pixel correlation of these tissue components in 3D (Figure 2A). If this correlation is high, then the sampling of a tumor can be sparse. As a limit, if this correlation is perfect, then a 2D section is sufficient to capture the composition of the tumor.

This correlation was calculated for each tissue component and for all WSIs spaced between 4 and 720 μm apart, averaged across the seven 3D tumor samples, and plotted as a function of distance (Figure 2B). Making intuitive sense, our analysis revealed that more abundant structures, such as extracellular matrix (ECM) and acini, remained spatially correlated over large

Resource



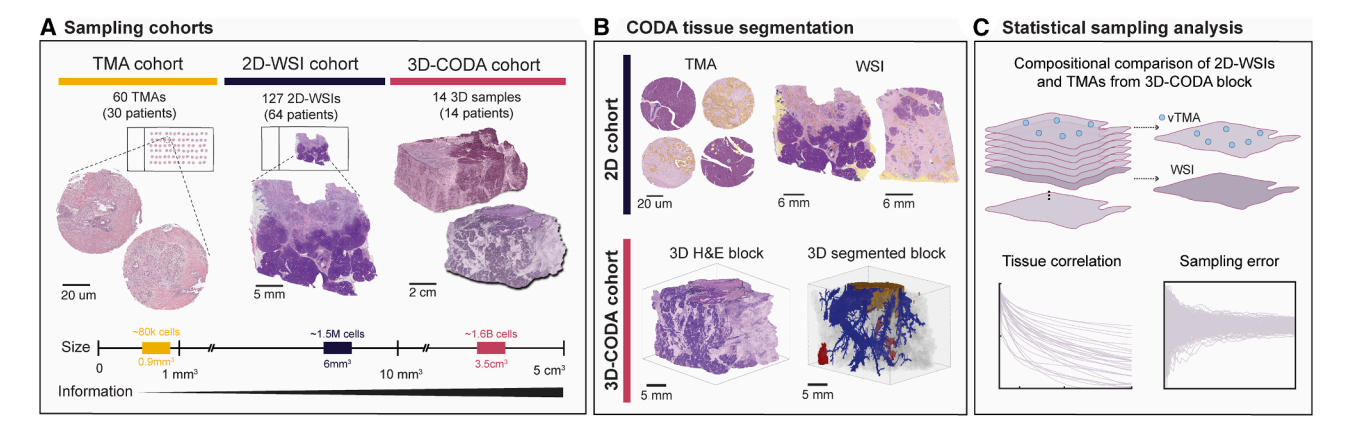


Figure 1. Overview of statistical sampling analysis for assessment of inter- and intra-patient tumor heterogeneity

(A) Cohorts of 14 3D blocks, 127 WSIs from 64 individuals, and a TMA containing cores from 30 samples were collected.

(B) Tissues were surgically resected, formalin fixed and paraffin embedded, sectioned, stained with H&E, and digitized. CODA segmentation was used to label 10 different microanatomical components at a resolution of 1 μm. For the processing of the 3D-CODA cohort, specimens were additionally registered into aligned tissue volumes.

(C) Statistical sampling analysis was conducted to assess the importance of sampling and associated sampling error.

distances within the blocks, requiring >180 slides (or $720 \mu m$) until they reached a spatial correlation that had decreased by >50%. For sparser tissues, such as nerves and vasculature, this correlation dropped by >50% within just 24 μm , or six 4-mm-thick slices (Figure 2C). Hence, tissue composition becomes rapidly decorrelated within pancreatic tumors.

To determine whether this rapid decorrelation holds in non-diseased organs, we conducted a similar analysis in seven 3D samples of grossly normal pancreas. Interestingly, the spatial correlation of ECM dropped more rapidly in normal tissue, with a loss of >50% in just 24 μm (compared to 720 μm in cancer tissue). As expected, we found that the spatial correlation in acinar tissue decayed more slowly in normal pancreas, reflecting the marked acinar atrophy and desmoplastic stromal deposition that occurs in pancreatic cancer.

We repeated this calculation for samples virtually cut to $6.5 \times 6.5 \, \text{mm}^2$, the area used in some spatial transcriptomics analyses (Figure S2). For tissue components such as ducts, PDAC, islets of Langerhans, blood vessels, nerves, and fat, a decrease in spatial correlation of 50% was observed within just 40 μ m, or 10 sections.

In conclusion, tissue composition changes rapidly in both normal and diseased tissues, highlighting the necessity of 3D assessments to fully capture their spatial organization.

Limitations of core-needle biopsies in assessment of tumor heterogeneity in tissue composition

TMA cores are often created following pathologist-selected ROIs on a single histological section that contains a target structure (e.g., cancer). Hundreds of sections may be subsequently cut from these cores for use by researchers who aim to study the original structure chosen by the pathologist. We hypothesized that due to the rapid changes in tissue composition across 3D tumors (Figure 2), the specific target structures and cellular features selected by pathologists in the initial ROIs could quickly be lost in the cores as successive sections

are cut. To quantify this, we created virtual cores within our 3D samples (Figure 3A). We manually chose 50 locations on the first H&E section of two 3D samples containing visually high cancer content. From these virtual cores, we digitally cut virtual TMA (vTMA) sections and quantified the change in tissue composition compared to the first (target) section (Figure 3B).

First, we considered the situation where researchers' objective is to profile the composition of the tumor microenvironment (Figure 3C). We quantified changes in stromal cell density across vTMA sections to assess whether the number and identity of stromal cells would vary greatly between slides, leading to the possibility that two researchers, studying sections from the same TMA cut hundreds of slides apart, could reach opposite conclusions. We found that, as subsequential sections are cut from the initial pathologist-selected ROI, stromal cell density errored, on average, 25% within the first 100 sections (0.4 mm), with many simulations nearing 100% change within 300 sections (~1.2 mm).

Finally, we determined the average number of virtual sections within which virtual cores lost their target structure altogether (Figure 3D). In this case, core ROIs were chosen as containing high cancer content. We thus determined how many of the 100 simulated cores no longer contained cancer for each virtual section. We found that nearly 50% of cores contained no cancer within 200 sections (0.8 mm), with this number approaching 75% after 300 sections.

This analysis demonstrates a rapid decorrelation in cancer content even within expert-guided cores, suggesting that TMA cores may rapidly lose the benefit of expert-guided ROI selection as sections are cut.

Hundreds of TMAs are necessary to capture the true tissue composition of WSIs and 3D tumors

Conventional histological analysis often relies on 2D tissue sections or TMAs to quantify the overall composition of tumors. While practical for large-scale studies, this approach assumes



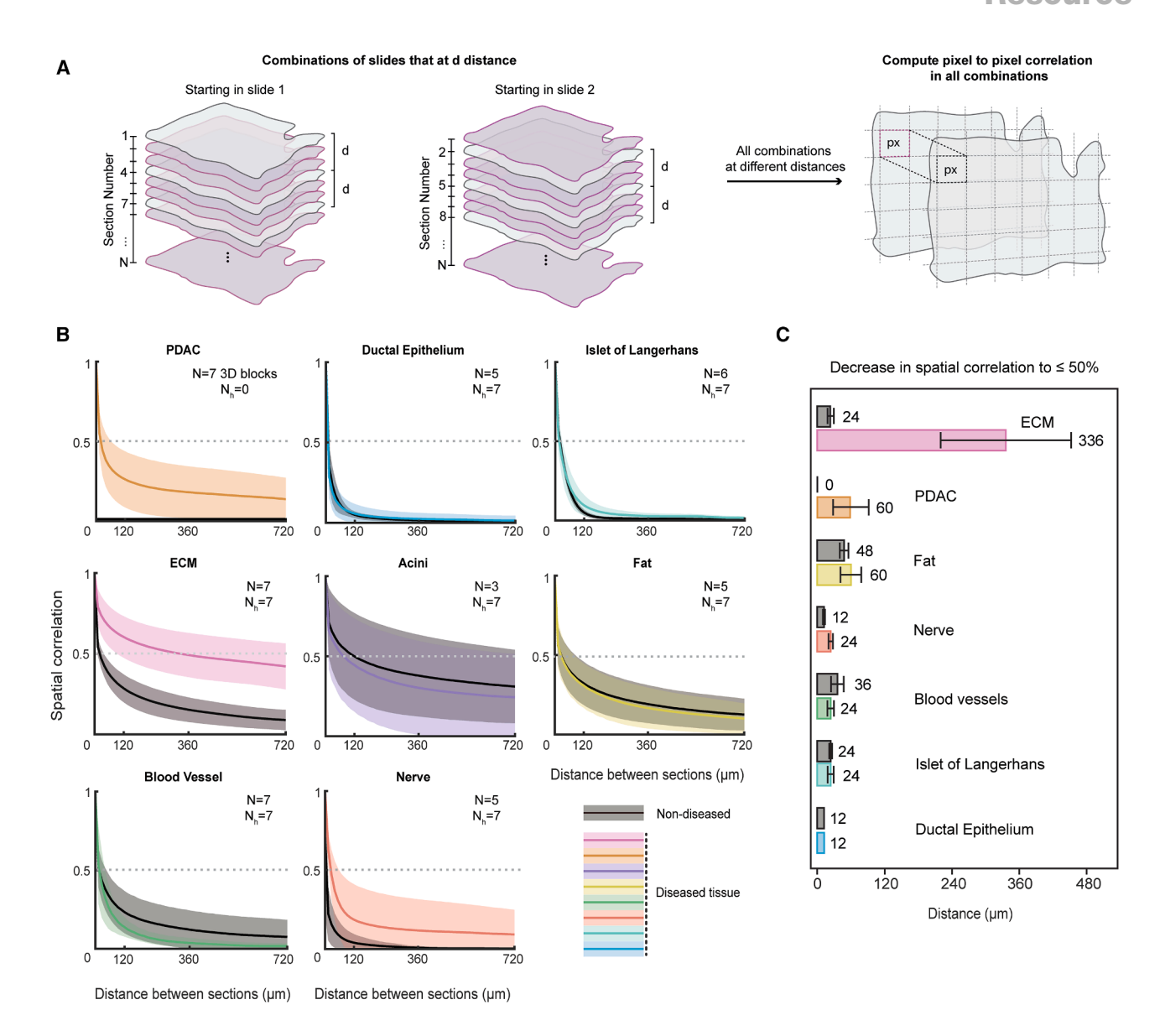


Figure 2. Quantifying the length scale of decay in spatial correlation of tumors

(A) 2D spatial correlation in tissue composition was determined for all combinations of pairs of sections in the 3D samples.

(B) For each tissue type, correlation was plotted as a function of distance between section pairs (line: mean across 3D samples, shaded area: standard deviation across 3D samples, colored plot: cancer samples, and gray: grossly normal samples).

(C) Distances at which the correlation falls below 50%, revealing that the length scale of compositional decorrelation in a normal and a cancer-containing pancreatic tissue is extremely short.

that these limited samples are representative of entire heterogeneous 3D tumors. This can lead to a significant loss of information, which can overlook important spatial tissue composition variations and miss rare cell populations. Here, we aimed to quantify information loss when subsampling a heterogeneous 3D sample through 2D histology. To do this, we randomly simulated vTMAs with a 1 mm diameter in the 2D WSIs and the 3D samples (Figure 4A). We quantified the error in tissue composition for various numbers of random, non-overlapping vTMAs compared to the true, 3D tissue composition (Figure 4B). This process was repeated to quantify the error between vTMAs

and 2D WSI composition (Figure 4C) and the error between 2D WSIs and 3D tissues (Figure 4D).

As expected, increasing the number of TMAs taken from a sample decreased the error of estimation of tissue composition of that sample, and this error varied across different microanatomical tissues (Figures 4B–4D). By comparing the number of 2D sections necessary to reach <10% error, we identified tissue components of high and low heterogeneity (Figures 4E–4G). We identified ECM as the component with the lowest heterogeneity, with an average of 19 TMAs necessary to reach <10% error in the estimation of 2D-WSI composition, 22 TMAs necessary for the

Resource



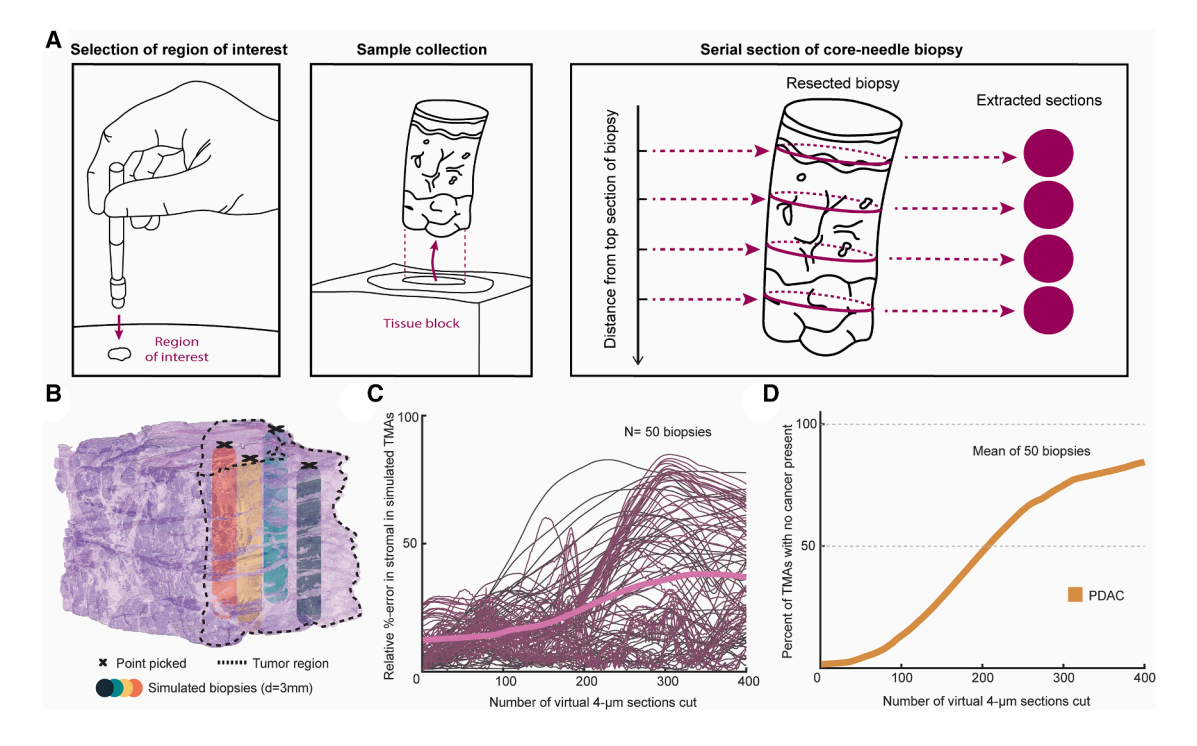


Figure 3. Error when TMA cores are used to assess spatial tissue content in a tumor

- (A) Cartoon demonstrating the process of region selection and tissue coring for creation of TMAs.
- (B) 50 ROIs containing cancer were manually selected from the top slide of two 3D samples.
- (C) TMAs were virtually cut and the relative error in stromal cell density in comparison to the original ROI was calculated.
- (D) TMAs were virtually cut and the percentage of TMAs with no cancer present on a given cut was calculated.

estimation of 3D-volume composition, and only 1 WSI necessary to correctly estimate 3D-volume composition (within 10% error). In contrast, we identified cancer as a much more heterogeneous structure, with >500 TMAs necessary to estimate the true 3D composition with <10% error.

We repeated this calculation for samples virtually cut to $6.5 \times 6.5 \text{ mm}^2$, the area often used in spatial transcriptomics analyses (Figure S2). 51–54 Our analysis demonstrated that tissue components such as acini, islets of Langerhans, PDAC, ducts, and blood vessels required roughly 50 simulated sections to estimate true 3D tissue composition with <10% error. Overall, this analysis demonstrates that subsampling heterogeneous tumors leads to significant information loss and that this information loss may be quantified through the simulation of 3D anatomical tissue maps.

Sampling guidelines in pancreatic cancer determined through 3D assessment of neoplastic content

In studies of pancreatic cancer initiation and its precursors (pancreatic intraepithelial neoplasias [PanlNs]), an accurate understanding of the number and composition of cancer precursors in the ductal system is necessary to determine the risk of a given precursor lesion to progress to cancer. ^{55–57} Yet, it is not currently feasible to profile entire human pancreases at cellular resolution to quantify all precursors. Here, we demonstrate that the amount of tissue necessary for incidence profiling may be estimated using simulations of 3D tissue. To do this, we

assessed the sampling necessary to reach a preset error in the estimation of neoplastic content.

For this calculation, we utilized a previously reported cohort of 48 large 3D reconstructed samples of human pancreas tissue containing PanlNs, the precursors to pancreatic cancer. We defined PanlN burden as the volume percent of PanlNs within the pancreatic ductal system. Next, we calculated PanlN burden for all possible combinations of consecutive slides subsampled from 3D and calculated the relative error of the subsampled region to that of the full 3D sample (Figure 5A). Visualizing this as bar plots for low, medium, and high PanlN burden revealed that fewer slides are needed to accurately determine the neoplastic content of samples containing extensive PanlNs, while many slides are needed to accurately determine the neoplastic content of samples containing fewer PanlNs (Figure 5B).

We conducted the same calculation for cancer content. We defined cancer burden as the percentage of epithelial cells that were classified as PDAC. Again, we found that fewer slides are needed to estimate the composition of cancer in samples with high cancer burden but that many slides are necessary to estimate cancer composition in samples with low neoplastic content (Figure 5C).

These results suggest the rather intuitive guideline that the rarer the tissue component being studied, the larger the number of sections required for a rigorous assessment of that component's content. This calculation may be used in the design of



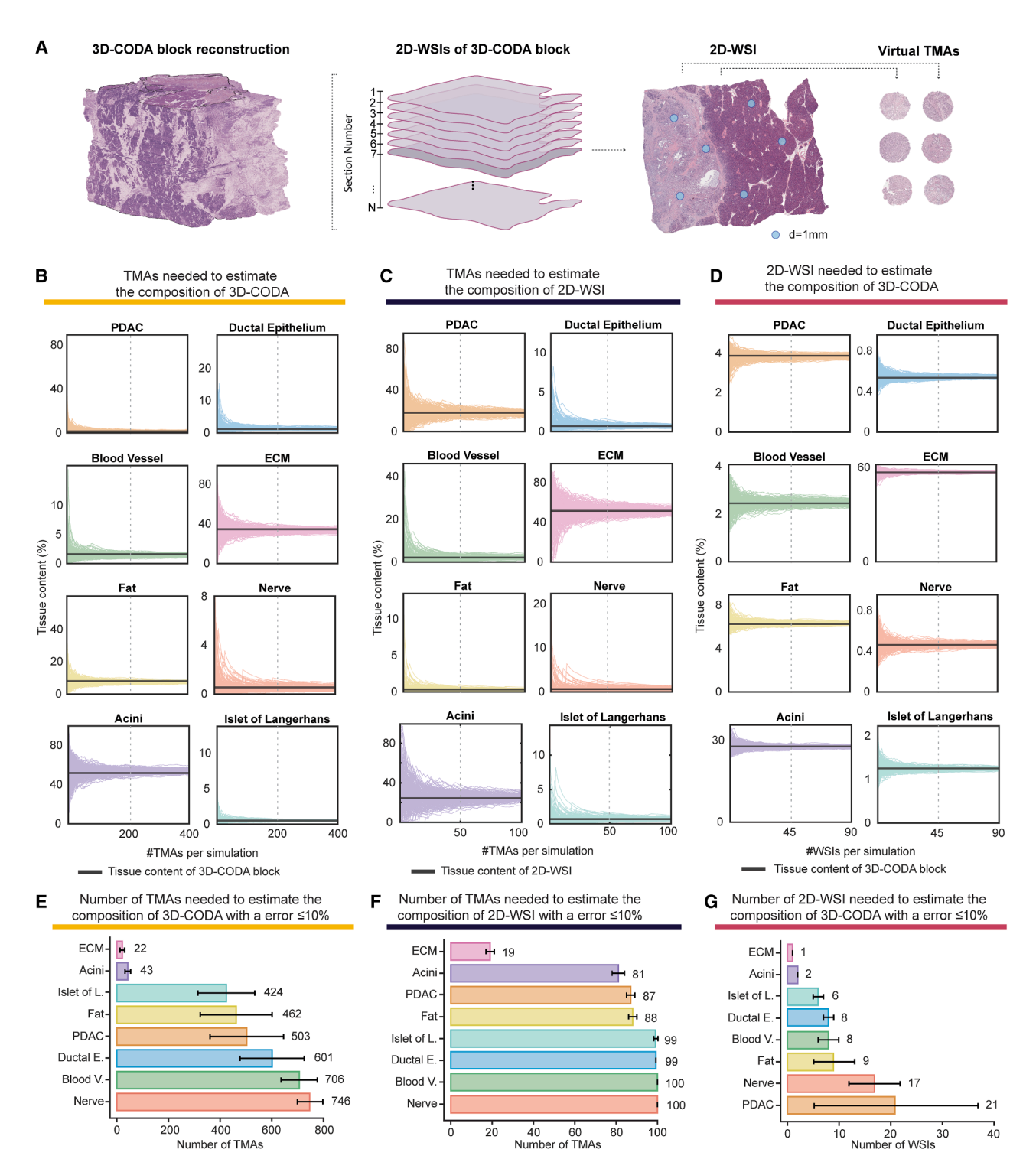


Figure 4. Hundreds of TMAs and tens of WSIs are needed to accurately estimate the true composition of 3D tumors

(A) Representation of 3D-CODA H&E-stained volume, comprised of serial, 2D-WSIs, from which virtual TMAs may be extracted.

(B) The loss in the accuracy of calculation of tissue composition due to TMA subsampling was measured through 200 simulations of 1–100 virtual TMAs (vTMAs) in the 2D-WSI cohort. Tissue composition of the generated vTMAs was compared to the average 2D-WSI (black line).

(legend continued on next page)

Resource



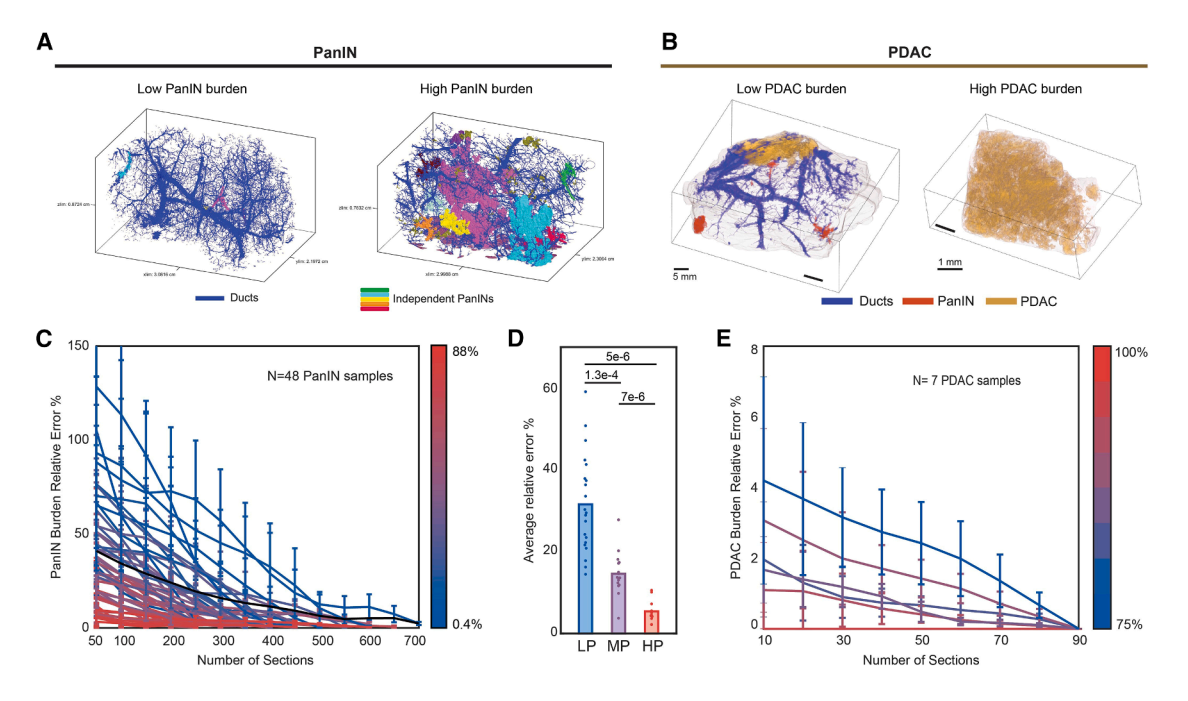


Figure 5. Quantification of error in estimation of neoplastic content when subsampling 3D tissues

(A and B) 3D renderings of pancreata containing (A) low or high PanIN content and (B) low or high PDAC content.

(C) For 48 3D samples containing PanINs (precursors to pancreatic cancer), the error in estimation of overall PanIN content plotted as a function of the number of consecutive sections subsampled. Lines are color coded according to the PanIN content of the 3D sample.

(D) The data in (C) binned according to overall PanIN content in equal thirds as low PanIN burden (0%–33%, LP), Moderate PanIN burden (34%–67%, MP), and high PanIN burden (68%–100%, HP) to show that fewer sections are needed to accurately estimate the PanIN content of samples that contain many PanIN lesions, and vice versa. p values: LP compared to MP = 1.3E–4; LP compared to HP = 5E–6; MP compared to HP = 7E–6.

(E) The calculation of (C) repeated for the seven samples containing PDAC to show that fewer sections are needed to accurately estimate cancer content in samples that contain high cancer composition. Data are represented as mean ± SEM.

studies seeking to minimize the amount of tissue collected for accurate estimation of rare structures.

DISCUSSION

Methods for spatially resolved cellular profiling have enabled indepth quantitative mapping of tissues and tumors to study interpatient and intra-patient differences in normal human anatomy and disease onset and progression. These methods profile extremely limited regions, which may impact the evaluation of tissue content and local heterogeneity due to tissue subsampling.

Here, we used CODA to quantitatively compare inter- and intrasample heterogeneity through the lens of tissue composition. Using the pancreas as a model system, we demonstrated that the correlation of tissue structures decays within tens of microns, even in normal tissues; that the target ROI selected by expert pathologists in the design of tissue cores may be rapidly lost within tens of sections; and that tens of WSIs and hundreds of TMAs are needed to recapitulate the true, 3D tissue composition. Further, we demonstrated that quantification of 3D-mapped tissues may be used to estimate the number of sections necessary for accurate 2D experimentation. Given that spatial heterogeneity is common in many tumors, similar patterns of rapid tissue structure decay and sampling challenges are also likely to be present in other cancers. To improve tissue analysis accuracy and reduce information loss, it is crucial to account for these subsampling factors.

While this work studies inter- and intra-tumoral heterogeneity through meticulous enumeration of tissue composition, it is likely that molecular, genomic, and transcriptomic heterogeneity is also high within 3D tissue samples. For example, recent work has shown that PanlNs (precursors to pancreatic cancer) exhibit great inter- and intra-lesional heterogeneity in KRAS mutations, suggesting that these lesions develop primarily from independent genetic events and may meet and merge within the ductal system. 5,46 Using CyCIF to measure cellular heterogeneity, groups have also shown alterations in marker-positive cells from TMAs to WSIs. 58

The impact of transitioning from 2D to 3D analysis has been shown to be important in clinically relevant features, such as

(C and D) The calculation of (A) was repeated for the calculation of (C) the loss in accuracy between TMAs and 3D tumors and (D) the loss in accuracy between 2D WSIs and 3D tumors.

(E–G) Distilling the information from the simulations shown in (A)–(C), we determined the number of TMAs and WSIs necessary to estimate WSI and 3D-tumor composition with \leq 10% error. Some structures, such as blood vessels, nerves, and PanINs, take tens to hundreds of 2D sections to reach \leq 10% error. Data are represented as mean \pm SEM.



the Gleason grade in prostate cancer, which can vary greatly across short distances of a 3D sample. \$^{16,27,30,58-64}\$ Additionally, recent work on pancreatic precursor lesions indicates that diagnostic criteria for intraductal papillary mucinous neoplasms (IPMNs), primarily based on 2D planar cross-sectional dimensions, may be inaccurate when moving to 3D, potentially requiring the reclassification of some lesions as PanINs. \$^{21}\$

Despite the potential of 3D imaging, its widespread adoption in basic and clinical research has been limited by high operational costs and the technical expertise necessary for sample processing, imaging, and computational analysis. However, several technological developments are reducing these barriers. The decreasing cost of chemical reagents for optical tissue clearing, 65–69 optimized software, 70,71 and the integration of generative artificial intelligence for interpolation of missing or damaged images in volumetric stacks are collectively enhancing scalability. The parallel, the emergence of open-source GUIs for light-sheet fluorescence microscopy and serial section histology reconstruction has accelerated the use of 3D in tissue analysis in biomedical and oncologic research. 38,73

In sum, we demonstrate in this work that 3D assessments are necessary to accurately assess tissue composition and tumor content and provide guidelines for the rate of sampling necessary to rigorously assess spatially resolved tissue composition and associated tissue density and intercellular distances.

Limitations of the study

This study primarily evaluates tissue composition heterogeneity and does not directly assess genomic, transcriptomic, or molecular variability, which also significantly contributes to spatial differences. The analysis was performed only on pancreatic tissue, potentially limiting the generalizability of the findings to other tissues or cancers. Additionally, the practical constraints of cost and specialized expertise required for the widespread adoption of 3D methodologies remain notable factors.

RESOURCE AVAILABILITY

Lead contact

Further information and requests for resources and reagents should be directed to and will be fulfilled by the lead contact, Denis Wirtz (wirtz@jh.edu).

Materials availability

This study did not generate new unique reagents.

Data and code availability

- The 3D dataset generated for this study is available in Zenodo (DOI: https://zenodo.org/records/15337577), as listed in the key resources table.
- The code used to generate the 3D tissue maps is available on the following GitHub (https://github.com/ashleylk/CODA) and Zenodo (https://zenodo. org/records/11130691, https://doi.org/10.1038/s41592-022-01650-9), as listed in the key resources table.
- Any additional information required to reanalyze the data reported in this
 work paper is available from the lead contact upon request.

ACKNOWLEDGMENTS

The authors acknowledge the following sources of support: U54CA268083 and UG3CA275681 grants from the National Cancer Institute; the Lustgarten Foundation-AACR Career Development Award for pancreatic cancer research

in honor of Ruth Bader Ginsburg; Susan Wojcicki and Dennis Troper; the Carl and Carol Nale Fund for Pancreatic Cancer Research; the Rolfe Pancreatic Cancer Foundation, and Johns Hopkins University and Instituto Superior Técnico exchange program (HOPTEC).

AUTHOR CONTRIBUTIONS

A.L.K. and D.W. conceived the project. A.L.K., A.M.B., K.F., T.C., S.-M.H., and R.H.H. collected and processed the human pancreas samples. A.L.K., A.F., E. V., S.J., V.M.R., A.C.J., and P.-S.W. conducted the image analysis and heterogeneity quantifications. S.-M.H., L.D.W., and R.H.H. validated histological analysis as clinical experts in pancreatic cancer pathology. A.F., A.L.K., R.H. H., and D.W. wrote the first draft of the manuscript, which all authors edited and approved.

DECLARATION OF INTERESTS

The authors declare no competing interests.

STAR*METHODS

Detailed methods are provided in the online version of this paper and include the following:

- KEY RESOURCES TABLE
- EXPERIMENTAL MODEL AND STUDY PARTICIPANT DETAILS
- METHOD DETAILS
 - o Computational resources
 - Tissue processing
 - o Segmentation of pancreatic microanatomy in 2D
 - o Reconstruction of pancreatic microanatomy in 3D
 - $\circ\,$ Calculation of variation in tissue composition in 2D and 3D
 - Calculation of the number of tissue microarrays necessary to understand WSI and 3D tissue composition
 - Calculation of the decay in spatial correlation within 2D and 3D samples
 - o Calculation of the change in tissue composition along vTMA cores
 - Calculation of the number of sections necessary to understand neoplastic content
- QUANTIFICATION AND STATISTICAL ANALYSIS

SUPPLEMENTAL INFORMATION

Supplemental information can be found online at https://doi.org/10.1016/j.crmeth.2025.101075.

Received: November 13, 2024 Revised: April 23, 2025 Accepted: May 16, 2025 Published: June 9, 2025

REFERENCES

- Liu, Y., Yang, M., Deng, Y., Su, G., Enninful, A., Guo, C.C., Tebaldi, T., Zhang, D., Kim, D., Bai, Z., et al. (2020). High-Spatial-Resolution Multi-Omics Sequencing via Deterministic Barcoding in Tissue. Cell 183, 1665–1681.e18. https://doi.org/10.1016/j.cell.2020.10.026.
- Ozsolak, F., and Milos, P.M. (2011). RNA sequencing: advances, challenges and opportunities. Nat. Rev. Genet. 12, 87–98. https://doi.org/10.1038/nrg2934.
- Pidsley, R., Zotenko, E., Peters, T.J., Lawrence, M.G., Risbridger, G.P., Molloy, P., Van Djik, S., Muhlhausler, B., Stirzaker, C., and Clark, S.J. (2016). Critical evaluation of the Illumina MethylationEPIC BeadChip microarray for whole-genome DNA methylation profiling. Genome Biol. 17, 208. https://doi.org/10.1186/s13059-016-1066-1.

Resource



- Cheng, M., Bhujwalla, Z.M., and Glunde, K. (2016). Targeting Phospholipid Metabolism in Cancer. Front. Oncol. 6, 266. https://doi.org/10.3389/fonc. 2016.00266.
- Braxton, A.M., Kiemen, A.L., Grahn, M.P., Forjaz, A., Parksong, J., Mahesh Babu, J., Lai, J., Zheng, L., Niknafs, N., Jiang, L., et al. (2024). 3D genomic mapping reveals multifocality of human pancreatic precancers. Nature 629, 679–687. https://doi.org/10.1038/s41586-024-07359-3.
- Bell, A.T.F., Mitchell, J.T., Kiemen, A.L., Lyman, M., Fujikura, K., Lee, J.W., Coyne, E., Shin, S.M., Nagaraj, S., Deshpande, A., et al. (2024). PanIN and CAF transitions in pancreatic carcinogenesis revealed with spatial data integration. cels 15, 753–769.e5. https://doi.org/10.1016/j.cels.2024. 07.001.
- Vogelstein, B., Papadopoulos, N., Velculescu, V.E., Zhou, S., Diaz, L.A., and Kinzler, K.W. (2013). Cancer Genome Landscapes. Science 339, 1546–1558. https://doi.org/10.1126/science.1235122.
- Lin, J.-R., Fallahi-Sichani, M., and Sorger, P.K. (2015). Highly multiplexed imaging of single cells using a high-throughput cyclic immunofluorescence method. Nat. Commun. 6, 8390. https://doi.org/10.1038/ ncomms9390.
- Angelo, M., Bendall, S.C., Finck, R., Hale, M.B., Hitzman, C., Borowsky, A. D., Levenson, R.M., Lowe, J.B., Liu, S.D., Zhao, S., et al. (2014). Multiplexed ion beam imaging of human breast tumors. Nat. Med. 20, 436–442. https://doi.org/10.1038/nm.3488.
- Goltsev, Y., Samusik, N., Kennedy-Darling, J., Bhate, S., Hale, M., Vazquez, G., Black, S., and Nolan, G.P. (2018). Deep Profiling of Mouse Splenic Architecture with CODEX Multiplexed Imaging. Cell 174, 968–981.e15. https://doi.org/10.1016/j.cell.2018.07.010.
- Kuett, L., Catena, R., Özcan, A., Plüss, A., Ali, H.R., Sa'd, M.A., Sa'd, M.A., Aparicio, S., Battistoni, G., Balasubramanian, S., et al. (2021). Threedimensional imaging mass cytometry for highly multiplexed molecular and cellular mapping of tissues and the tumor microenvironment. Nat. Cancer 3, 122–133. https://doi.org/10.1038/s43018-021-00301-w.
- Eng, C.-H.L., Lawson, M., Zhu, Q., Dries, R., Koulena, N., Takei, Y., Yun, J., Cronin, C., Karp, C., Yuan, G.-C., and Cai, L. (2019). Transcriptome-scale super-resolved imaging in tissues by RNA seqFISH+. Nature 568, 235–239. https://doi.org/10.1038/s41586-019-1049-y.
- Xia, C., Fan, J., Emanuel, G., Hao, J., and Zhuang, X. (2019). Spatial transcriptome profiling by MERFISH reveals subcellular RNA compartmentalization and cell cycle-dependent gene expression. Proc. Natl. Acad. Sci. USA 116, 19490–19499. https://doi.org/10.1073/pnas.1912459116.
- Bressan, D., Battistoni, G., and Hannon, G.J. (2023). The dawn of spatial omics. Science 381, eabq4964. https://doi.org/10.1126/science. abq4964
- Senter-Zapata, M., Patel, K., Bautista, P.A., Griffin, M., Michaelson, J., and Yagi, Y. (2016). The Role of Micro-CT in 3D Histology Imaging. Pathobiology 83, 140–147. https://doi.org/10.1159/000442387.
- Liu, J.T., Chow, S.S., Colling, R., Downes, M.R., Farré, X., Humphrey, P., Janowczyk, A., Mirtti, T., Verrill, C., Zlobec, I., and True, L.D. (2024). Engineering the future of 3D pathology. J. Pathol. Clin. Res. 10, e347. https://doi.org/10.1002/cjp2.347.
- Kiemen, A.L., Braxton, A.M., Grahn, M.P., Han, K.S., Babu, J.M., Reichel, R., Jiang, A.C., Kim, B., Hsu, J., Amoa, F., et al. (2022). CODA: quantitative 3D reconstruction of large tissues at cellular resolution. Nat. Methods 19, 1490–1499. https://doi.org/10.1038/s41592-022-01650-9.
- Gatenbee, C.D., Baker, A.-M., Prabhakaran, S., Swinyard, O., Slebos, R.J. C., Mandal, G., Mulholland, E., Andor, N., Marusyk, A., Leedham, S., et al. (2023). Virtual alignment of pathology image series for multi-gigapixel whole slide images. Nat. Commun. 14, 4502. https://doi.org/10.1038/ s41467-023-40218-9.
- Fischer, A.H., Jacobson, K.A., Rose, J., and Zeller, R. (2008). Hematoxylin and Eosin Staining of Tissue and Cell Sections. CSH Protoc. 2008, pdb. prot4986. https://doi.org/10.1101/pdb.prot4986.

- Matos, L.L.d., Trufelli, D.C., De Matos, M.G.L., and Da Silva Pinhal, M.A. (2010). Immunohistochemistry as an Important Tool in Biomarkers Detection and Clinical Practice. Biomark 5, S2185. https://doi.org/10.4137/BMI. S2185.
- Kiemen, A.L., Dequiedt, L., Shen, Y., Zhu, Y., Matos-Romero, V., Forjaz, A., Campbell, K., Dhana, W., Cornish, T., Braxton, A.M., et al. (2024). PanIN or IPMN? Redefining Lesion Size in 3 Dimensions. Am. J. Surg. Pathol. 48, 839–845. https://doi.org/10.1097/PAS.0000000000002245.
- Gao, G., Song, A.H., Wang, F., Brenes, D., Wang, R., Chow, S.S.L., Bishop, K.W., True, L.D., Mahmood, F., and Liu, J.T.C. (2024). Triage of 3D pathology data via 2.5D multiple-instance learning to guide pathologist assessments. Preprint at arxiv. https://arxiv.org/html/2406.07061v1.
- Winetraub, Y., Yuan, E., Terem, I., Yu, C., Chan, W., Do, H., Shevidi, S., Mao, M., Yu, J., Hong, M., et al. (2021). OCT2Hist: Non-Invasive Virtual Biopsy Using Optical Coherence Tomography. Preprint at medRxiv. https:// doi.org/10.1101/2021.03.31.21254733.
- Song, A.H., Williams, M., Williamson, D.F.K., Jaume, G., Zhang, A., Chen, B., Serafin, R., Liu, J.T.C., Baras, A., Parwani, A.V., et al. (2023). Weakly Supervised Al for Efficient Analysis of 3D Pathology Samples. Preprint at ArXiv. https://doi.org/10.1016/j.cell.2024.03.035.
- Susaki, E.A., Tainaka, K., Perrin, D., Kishino, F., Tawara, T., Watanabe, T. M., Yokoyama, C., Onoe, H., Eguchi, M., Yamaguchi, S., et al. (2014). Whole-Brain Imaging with Single-Cell Resolution Using Chemical Cocktails and Computational Analysis. Cell 157, 726–739. https://doi.org/10.1016/j.cell.2014.03.042.
- Hong, S.-M., Jung, D., Kiemen, A., Gaida, M.M., Yoshizawa, T., Braxton, A.M., Noë, M., Lionheart, G., Oshima, K., Thompson, E.D., et al. (2020). Three-dimensional visualization of cleared human pancreas cancer reveals that sustained epithelial-to-mesenchymal transition is not required for venous invasion. Mod. Pathol. 33, 639–647. https://doi.org/10.1038/ s41379-019-0409-3.
- Koyuncu, C., Janowczyk, A., Farre, X., Pathak, T., Mirtti, T., Fernandez, P. L., Pons, L., Reder, N.P., Serafin, R., Chow, S.S.L., et al. (2023). Visual Assessment of 2-Dimensional Levels Within 3-Dimensional Pathology Data Sets of Prostate Needle Biopsies Reveals Substantial Spatial Heterogeneity. Lab. Invest. 103, 100265. https://doi.org/10.1016/j.labinv.2023. 100265.
- Crawford, A.J., Forjaz, A., Bons, J., Bhorkar, I., Roy, T., Schell, D., Queiroga, V., Ren, K., Kramer, D., Huang, W., et al. (2024). Combined assembloid modeling and 3D whole-organ mapping captures the microanatomy and function of the human fallopian tube. Sci. Adv. 10, eadp6285. https://doi.org/10.1126/sciadv.adp6285.
- Kiemen, A.L., Damanakis, A.I., Braxton, A.M., He, J., Laheru, D., Fishman, E.K., Chames, P., Pérez, C.A., Wu, P.-H., Wirtz, D., et al. (2023). Tissue clearing and 3D reconstruction of digitized, serially sectioned slides provide novel insights into pancreatic cancer. Med 4, 75–91. https://doi. org/10.1016/j.medj.2022.11.009.
- Bishop, K.W., Erion Barner, L.A., Han, Q., Baraznenok, E., Lan, L., Poudel, C., Gao, G., Serafin, R.B., Chow, S.S.L., Glaser, A.K., et al. (2024). An end-to-end workflow for nondestructive 3D pathology. Nat. Protoc. 19, 1122–1148. https://doi.org/10.1038/s41596-023-00934-4.
- Kiemen, A.L., Forjaz, A., Sousa, R., Han, K.S., Hruban, R.H., Wood, L.D., Wu, P., and Wirtz, D. (2024). High-Resolution 3D Printing of Pancreatic Ductal Microanatomy Enabled by Serial Histology. Adv. Materials Technol. 9, 2301837.
- 32. Tempest, N., Jansen, M., Baker, A.M., Hill, C.J., Hale, M., Magee, D., Treanor, D., Wright, N.A., and Hapangama, D.K. (2020). Histological 3D reconstruction and in vivo lineage tracing of the human endometrium. J. Pathol. 251, 440–451.
- Barmpoutis, P., Di Capite, M., Kayhanian, H., Waddingham, W., Alexander, D.C., Jansen, M., and Kwong, F.N.K. (2021). Tertiary lymphoid structures (TLS) identification and density assessment on H&E-stained digital slides of lung cancer. PLoS One 16, e0256907.



Cell Reports Methods Resource

- Kiemen, A.L., Dbouk, M., Abou Diwan, E., Forjaz, A., Dequiedt, L., Baghdadi, A., Madani, S.P., Grahn, M.P., Jones, C., and Vedula, S. (2024). Magnetic Resonance Imaging–Based Assessment of Pancreatic Fat Strongly Correlates With Histology-Based Assessment of Pancreas Composition. Pancreas 53, e180–e186.
- Liu, J.T.C., Glaser, A.K., Bera, K., True, L.D., Reder, N.P., Eliceiri, K.W., and Madabhushi, A. (2021). Harnessing non-destructive 3D pathology. Nat. Biomed. Eng. 5, 203–218.
- Onozato, M.L., Klepeis, V.E., Yagi, Y., and Mino-Kenudson, M. (2012). A role of three-dimensional (3D)-reconstruction in the classification of lung adenocarcinoma. Anal. Cell. Pathol. 35, 79–84.
- Langer, E.M., Allen-Petersen, B.L., King, S.M., Kendsersky, N.D., Turnidge, M.A., Kuziel, G.M., Riggers, R., Samatham, R., Amery, T.S., Jacques, S.L., et al. (2019). Modeling tumor phenotypes in vitro with three-dimensional bioprinting. Cell Rep. 26, 608–623.e6.
- Matos-Romero, V., Gómez-Becerril, J., Forjaz, A., Dequiedt, L., Newton, T., Joshi, S., Shen, Y., Hanna, E., Nair, P., Sivasubramanian, A., et al. (2025). CODAvision: best practices and a user-friendly interface for rapid, customizable segmentation of medical images. Preprint at bioRxiv. https://doi.org/10.1101/2025.04.11.648464.
- Xue, Y., Lyu, C., Taylor, A., Van Ee, A., Kiemen, A., Choi, Y., Khavanian, N., Henn, D., Lee, C., Hwang, L., et al. (2022). Mechanical tension mobilizes Lgr6+ epidermal stem cells to drive skin growth. Sci. Adv. 8, eabl8698. https://doi.org/10.1126/sciadv.abl8698.
- Yang, H., Karl, M.N., Wang, W., Starich, B., Tan, H., Kiemen, A., Pucsek, A. B., Kuo, Y.-H., Russo, G.C., Pan, T., et al. (2022). Engineered bispecific antibodies targeting the interleukin-6 and -8 receptors potently inhibit cancer cell migration and tumor metastasis. Mol. Ther. 30, 3430–3449. https://doi.org/10.1016/j.ymthe.2022.07.008.
- Forjaz, A., Kramer, D., Shen, Y., Bea, H., Tsapatsis, M., Ping, J., Queiroga, V., San, K.H., Joshi, S., Grubel, C., et al. (2025). Integration of nuclear morphology and 3D imaging to profile cellular neighborhoods. Preprint at bioRxiv. https://doi.org/10.1101/2025.03.31.646356.
- O'Brien, J., Niehaus, P., Chang, K., Remark, J., Barrett, J., Dasgupta, A., Adenegan, M., Salimian, M., Kevas, Y., Chandrasekaran, K., et al. (2024). Skin keratinocyte-derived SIRT1 and BDNF modulate mechanical allodynia in mouse models of diabetic neuropathy. Brain 147, 3471–3486. https://doi.org/10.1093/brain/awae100.
- Kiemen, A.L., Choi, Y., Braxton, A.M., Almagro Pérez, C., Graham, S., Grahn, M.P., Nanda, N., Roberts, N., Wood, L., Wu, P., et al. (2023). Intraparenchymal metastases as a cause for local recurrence of pancreatic cancer. Histopathology (Oxf.) 82, 504–506. https://doi.org/10.1111/his. 14839.
- de Groot, A.E., Myers, K.V., Krueger, T.E.G., Kiemen, A.L., Nagy, N.H., Brame, A., Torres, V.E., Zhang, Z., Trabzonlu, L., Brennen, W.N., et al. (2021). Characterization of tumor-associated macrophages in prostate cancer transgenic mouse models. Prostate 81, 629–647. https://doi.org/ 10.1002/pros.24139.
- Sneider, A., Kiemen, A., Kim, J.H., Wu, P.-H., Habibi, M., White, M., Phillip, J.M., Gu, L., and Wirtz, D. (2022). Deep learning identification of stiffness markers in breast cancer. Biomaterials 285, 121540. https://doi.org/10. 1016/j.biomaterials.2022.121540.
- Kiemen, A.L., Almagro-Pérez, C., Matos, V., Forjaz, A., Braxton, A.M., Dequiedt, L., Parksong, J., Cannon, C.D., Yuan, X., Shin, S.M., et al. (2024).
 D histology reveals that immune response to pancreatic precancers is heterogeneous and depends on global pancreas structure. Preprint at bio-Rxiv. https://doi.org/10.1101/2024.08.03.606493.
- Kathiriya, I.S., Dominguez, M.H., Rao, K.S., Muncie-Vasic, J.M., Devine, W.P., Hu, K.M., Hota, S.K., Garay, B.I., Quintero, D., and Goyal, P. (2024). A disrupted compartment boundary underlies abnormal cardiac patterning and congenital heart defects. Preprint at bioRxiv. https://doi. org/10.1101/2024.02.05.578995.
- 48. Steele, N.G., Carpenter, E.S., Kemp, S.B., Sirihorachai, V.R., The, S., Delrosario, L., Lazarus, J., Amir, E.A.D., Gunchick, V., Espinoza, C., et al.

- (2020). Multimodal mapping of the tumor and peripheral blood immune landscape in human pancreatic cancer. Nat. Cancer *1*, 1097–1112. https://doi.org/10.1038/s43018-020-00121-4.
- Wang, L., Gaddam, S., Wang, N., Xie, Y., Deng, Z., Zhou, Z., Fan, Z., Jiang, T., Christodoulou, A.G., Han, F., et al. (2020). Multiparametric Mapping Magnetic Resonance Imaging of Pancreatic Disease. Front. Physiol. 11, 8. https://doi.org/10.3389/fphys.2020.00008.
- Raphael, B.J., Hruban, R.H., Aguirre, A.J., Moffitt, R.A., Yeh, J.J., Stewart, C., Robertson, A.G., Cherniack, A.D., Gupta, M., Getz, G., et al. (2017). Integrated genomic characterization of pancreatic ductal adenocarcinoma. Cancer Cell 32, 185–203.e13.
- Moncada, R., Barkley, D., Wagner, F., Chiodin, M., Devlin, J.C., Baron, M., Hajdu, C.H., Simeone, D.M., and Yanai, I. (2020). Integrating microarraybased spatial transcriptomics and single-cell RNA-seq reveals tissue architecture in pancreatic ductal adenocarcinomas. Nat. Biotechnol. 38, 333–342. https://doi.org/10.1038/s41587-019-0392-8.
- Johnson, J.A.I., Stein-O'Brien, G.L., Booth, M., Heiland, R., Kurtoglu, F., Bergman, D.R., Bucher, E., Deshpande, A., Forjaz, A., Getz, M., et al. (2023). Digitize your Biology! Modeling multicellular systems through interpretable cell behavior. Preprint at bioRxiv. https://doi.org/10.1101/2023. 09.17.557982.
- 53. He, B., Bergenstråhle, L., Stenbeck, L., Abid, A., Andersson, A., Borg, Å., Maaskola, J., Lundeberg, J., and Zou, J. (2020). Integrating spatial gene expression and breast tumour morphology via deep learning. Nat. Biomed. Eng. 4, 827–834. https://doi.org/10.1038/s41551-020-0578-x.
- Longo, S.K., Guo, M.G., Ji, A.L., and Khavari, P.A. (2021). Integrating single-cell and spatial transcriptomics to elucidate intercellular tissue dynamics. Nat. Rev. Genet. 22, 627–644. https://doi.org/10.1038/s41576-021-00370-8
- Distler, M., Aust, D., Weitz, J., Pilarsky, C., and Grützmann, R. (2014). Precursor Lesions for Sporadic Pancreatic Cancer: PanIN, IPMN, and MCN. BioMed Res. Int. 2014, 474905. https://doi.org/10.1155/2014/474905.
- Lennon, A.M., Wolfgang, C.L., Canto, M.I., Klein, A.P., Herman, J.M., Goggins, M., Fishman, E.K., Kamel, I., Weiss, M.J., Diaz, L.A., et al. (2014). The Early Detection of Pancreatic Cancer: What Will It Take to Diagnose and Treat Curable Pancreatic Neoplasia? Cancer Res. 74, 3381–3389. https://doi.org/10.1158/0008-5472.CAN-14-0734.
- McGuigan, A., Kelly, P., Turkington, R.C., Jones, C., Coleman, H.G., and McCain, R.S. (2018). Pancreatic cancer: A review of clinical diagnosis, epidemiology, treatment and outcomes. World J. Gastroenterol. 24, 4846–4861. https://doi.org/10.3748/wjg.v24.i43.4846.
- 58. Lin, J.-R., Wang, S., Coy, S., Chen, Y.-A., Yapp, C., Tyler, M., Nariya, M.K., Heiser, C.N., Lau, K.S., Santagata, S., and Sorger, P.K. (2023). Multiplexed 3D atlas of state transitions and immune interaction in colorectal cancer. Cell 186, 363–381.e19. https://doi.org/10.1016/j.cell.2022.12.028.
- 59. Song, A.H., Williams, M., Williamson, D.F.K., Chow, S.S.L., Jaume, G., Gao, G., Zhang, A., Chen, B., Baras, A.S., Serafin, R., et al. (2024). Analysis of 3D pathology samples using weakly supervised Al. Cell 187, 2502–2520.e17. https://doi.org/10.1016/j.cell.2024.03.035.
- Serafin, R., Koyuncu, C., Xie, W., Huang, H., Glaser, A.K., Reder, N.P., Janowczyk, A., True, L.D., Madabhushi, A., and Liu, J.T. (2023). Nondestructive 3D pathology with analysis of nuclear features for prostate cancer risk assessment. J. Pathol. 260, 390–401. https://doi.org/10.1002/path.6090.
- Marx, V. (2023). Researchers dig into cancer niches. Nat. Methods 20, 484–488. https://doi.org/10.1038/s41592-023-01834-x.
- 62. Coy, S., Cheng, B., Lee, J.S., Rashid, R., Browning, L., Xu, Y., Chakrabarty, S.S., Yapp, C., Chan, S., Tefft, J.B., et al. (2023). 2D and 3D multiplexed subcellular profiling of nuclear instability in human cancer. Preprint at bioRxiv. https://doi.org/10.1101/2023.11.07.566063.
- 63. Fukui, H., Hori, M., Fukuda, Y., Onishi, H., Nakamoto, A., Ota, T., Ogawa, K., Ninomiya, K., Tatsumi, M., Osuga, K., et al. (2019). Evaluation of fatty pancreas by proton density fat fraction using 3-T magnetic resonance

Cell Reports Methods

Resource



- imaging and its association with pancreatic cancer. Eur. J. Radiol. 118, 25–31. https://doi.org/10.1016/j.ejrad.2019.06.024.
- Katsamenis, O.L., Olding, M., Warner, J.A., Chatelet, D.S., Jones, M.G., Sgalla, G., Smit, B., Larkin, O.J., Haig, I., Richeldi, L., et al. (2019). X-ray Micro-Computed Tomography for Nondestructive Three-Dimensional (3D) X-ray Histology. Am. J. Pathol. 189, 1608–1620. https://doi.org/10. 1016/j.ajpath.2019.05.004.
- Lee, B., Lee, J.-H., Kim, D.H., Kim, E.S., Seo, B.K., Rhyu, I.J., and Sun, W. (2022). MAX: a simple, affordable, and rapid tissue clearing reagent for 3D imaging of wide variety of biological specimens. Sci. Rep. 12, 19508. https://doi.org/10.1038/s41598-022-23376-6.
- Kim, K., Na, M., Oh, K., Cho, E., Han, S.S., and Chang, S. (2022). Optimized single-step optical clearing solution for 3D volume imaging of biological structures. Commun. Biol. 5, 431–510. https://doi.org/10.1038/s42003-022-03388-8.
- 67. Tomer, R., Ye, L., Hsueh, B., and Deisseroth, K. (2014). Advanced CLARITY for rapid and high-resolution imaging of intact tissues. Nat. Protoc. 9, 1682–1697. https://doi.org/10.1038/nprot.2014.123.
- Glaser, A.K., Reder, N.P., Chen, Y., Yin, C., Wei, L., Kang, S., Barner, L.A., Xie, W., McCarty, E.F., Mao, C., et al. (2019). Multi-immersion open-top light-sheet microscope for high-throughput imaging of cleared tissues. Nat. Commun. 10, 2781. https://doi.org/10.1038/s41467-019-10534-0.
- Ku, T., Guan, W., Evans, N.B., Sohn, C.H., Albanese, A., Kim, J.-G., Frosch, M.P., and Chung, K. (2020). Elasticizing tissues for reversible shape transformation and accelerated molecular labeling. Nat. Methods 17, 609–613. https://doi.org/10.1038/s41592-020-0823-y.
- Vladimirov, N., Voigt, F.F., Naert, T., Araujo, G.R., Cai, R., Reuss, A.M., Zhao, S., Schmid, P., Hildebrand, S., Schaettin, M., et al. (2024). Benchtop

- mesoSPIM: a next-generation open-source light-sheet microscope for cleared samples. Nat. Commun. *15*, 2679. https://doi.org/10.1038/s41467-024-46770-2.
- Otomo, K., Omura, T., Nozawa, Y., Edwards, S.J., Sato, Y., Saito, Y., Yagishita, S., Uchida, H., Watakabe, Y., Naitou, K., et al. (2024). descSPIM: an affordable and easy-to-build light-sheet microscope optimized for tissue clearing techniques. Nat. Commun. 15, 4941. https://doi.org/10.1038/s41467-024-49131-1.
- Joshi, S., Forjaz, A., Han, K.S., Shen, Y., Queiroga, V., Selaru, F.A., Gérard, M., Xenes, D., Matelsky, J., Wester, B., et al. (2025). InterpolAl: deep learning-based optical flow interpolation and restoration of biomedical images for improved 3D tissue mapping. Nat. Methods. https://doi.org/10.1038/s41592-025-02712-4
- Marin, Z., Wang, X., Collison, D.W., McFadden, C., Lin, J., Borges, H., Chen, B., Mehra, D., Shen, Q., Galecki, S., et al. (2024). navigate: an open-source platform for smart light-sheet microscopy. Nat. Methods 21, 1967–1969. https://doi.org/10.1101/2024.02.09.579083.
- Fujikura, K., Hutchings, D., Braxton, A.M., Zhu, Q., Laheru, D.A., Hruban, R.H., Thompson, E.D., and Wood, L.D. (2020). Intraductal pancreatic cancer is less responsive than cancer in the stroma to neoadjuvant chemotherapy. Mod. Pathol. 33, 2026–2034. https://doi.org/10.1038/s41379-020-0572-6.
- Chen, L.-C., Papandreou, G., Kokkinos, I., Murphy, K., and Yuille, A.L. (2016). DeepLab: Semantic Image Segmentation with Deep Convolutional Nets, Atrous Convolution, and Fully Connected CRFs. Preprint at arxiv. https://doi.org/10.48550/ARXIV.1606.00915.



Cell Reports Methods Resource

STAR*METHODS

KEY RESOURCES TABLE

REAGENT or RESOURCE	SOURCE	IDENTIFIER
Biological samples		
Tissue Microarray of human pancreas	TissueArray	PA803
Adult human pancreas	This paper	N/A
Chemicals, peptides, and recombinant proteins		
Molecular biology grade water	Corning	Catalog #46-000-CI
Xylene, Histological Grade	Milipore Sigma	Catalog #534056
Hematoxylin Solution, Mayer's	Milipore Sigma	Catalog #MHS16
Bluing reagent	Dako	Catalog #CS70230-2
Ethyl Alcohol, Pure (200proof, anhydrous)	Milipore Sigma	Catalog #E7023-500ML
Eosin Y-solution, Alcoholic	Milipore Sigma	Catalog #HT110116
Deposited data		
3D human pancreas CODA blocks	This paper	Zenodo: doi: https://zenodo.org/records/ 15337577
Software and algorithms		
Openslide	Goode et al.	https://github.com/openslide/openslide
Imagescope	Leica	https://www.leicabiosystems.com/us/digitalpathology/manage/aperio-imagescope/
CODA	Kiemen et al.	Zenodo: doi: https://zenodo.org/records/ 11130691
MATLAB	The MathWorks Inc.	https://www.mathworks.com
Other		
NanoZoomer S210	Hamamatsu	Catalog #C13239-01

EXPERIMENTAL MODEL AND STUDY PARTICIPANT DETAILS

This retrospective study was approved by the Institutional Review Board (IRB) at the Johns Hopkins University School of Medicine. Human pancreatic tissue specimens were analyzed across three independent cohorts: a commercially acquired tissue microarray (TMA), whole-slide images (WSI), and a three-dimensionally reconstructed specimens processed using the CODA imaging pipeline. ¹⁷ All samples were obtained from archived, de-identified surgical resections and used in accordance with institutional ethical regulations and informed consent protocols.

The TMA cohort consisted of 60 cores, each 1.5 mm in diameter, sampled from the pancreata of 30 individuals with pancreatic cancer. Each case was represented by two cores. The patients ranged in age from 40 to 84 years, with a mean of 58.4 years and a median of 60 years. Equal numbers of 30 male and 30 female donors were included in this group. These samples were obtained from a commercial vendor TissueArray. The WSI cohort comprises 64 surgical resections from patients treated at Johns Hopkins Hospital for pancreatic cancer, and is a cohort that was previously published. One representative FFPE slide per case was analyzed. Patient ages in this group ranged from 48 to 90 years, with a mean age of 64.4 years and a median age of 67 years. Of the patients, 22 were female and 25 were male, and gender information was not available for 17 individuals. The 3D-CODA cohort included pancreas resections from 14 individuals, also treated at Johns Hopkins Hospital, and is a cohort that was previously published. Seven of these samples were processed using serial sectioning, computational alignment, and microanatomical segmentation for 3D reconstruction. The mean number of histological sections per case was 393 slides, with a total of 5,503 images across the cohort. Patient ages ranged from 41 to 75 years, with a mean of 61.4 and a median of 58 years. Six of the patients were female and eight were male. Histological. Sex and age data are summarized in Table S1. All tissue handling and data analysis procedures conformed to institutional and national research standards.

METHOD DETAILS

Computational resources

For the execution of computational methods in this work, we used a computer with the following specifications: Intel i9 12th gen CPU, 128GB DDR4 memory RAM, and 3090 RTX Nvidia GPU. For implementation of the workflow by bench scientists, the CODA workflow

Cell Reports Methods

Resource



has been modularly optimized to support scalability and accessibility, allowing streamlined execution on standard laptop configurations with reduced computational overhead.³⁸

Tissue processing

Resected tissues were formalin-fixed, paraffin embedded, and sectioned at a thickness of $4 \mu m$. For the TMA and 2D-WSI cohorts, a single histological section was stained with H&E. For the 3D-CODA cohort, a minimum of 270 serial sections were taken, and every third section was stained with H&E, for a minimum of 90 H&E-stained tissue sections per sample. H&E-stained images were digitized at $20 \times magnification$ using a Hamamatsu S360 scanner.

Segmentation of pancreatic microanatomy in 2D

A previously developed deep learning semantic segmentation pipeline for the labeling of distinct microanatomical components in histological images was adapted here to label ten microanatomical components of human pancreatic cancer histology at 1 μ m per pixel resolution: pancreatic cancer, pancreatic cancer precursor lesions, normal ductal epithelium, acinar tissue, islets of Langerhans, vasculature, nerves, fat, and extracellular matrix (ECM). Convolutional neural networks were trained in MATLAB2023b to classify the TMA cores, 2D-WSI, and 3D-CODA cohorts of tissues. Manual annotations of the ten microanatomical tissue components were generated on a subset of histological images, and fed into the CODA-segmentation workflow for retraining of a resnet-50 network. Resulting networks were deemed acceptable if the overall accuracy exceeded 90% and minimum per-class precision and recall exceeded 85%.

Reconstruction of pancreatic microanatomy in 3D

CODA image registration was used to create digital tissue volumes from the serial H&E images for the seven samples in the 3D-CODA cohort. ¹⁷ This nonlinear registration workflow iteratively aligns serial stacks of images (with the reference coordinates at the center of the stack), and utilizes a two-step global and local calculation in MATLAB2023b. Images are downsampled to a resolution of eight μ m per pixel, converted to greyscale, and Gaussian-filtered. Global registration angle is calculated through maximization of the cross correlation of radon-transforms of the filtered images taken at discrete angles from 0° to 360°, and registration translation is calculated through maximization of the cross correlation of the rotated, filtered images. Local registration is computed by repeating this process along subsampled regions of the two globally registered images. This registration is repeated for all images in the serial samples and is subsequently rescaled and applied to the high resolution (1 μ m per pixel resolution) H&E and microanatomically segmented H&E images.

Calculation of variation in tissue composition in 2D and 3D

For each discrete sample in the TMA, 2D-WSI and 3D-CODA cohort, overall microanatomical composition was assessed. First, the number of pixels classified as each of the 10 microanatomical tissue types segmented by the deep learning model was determined. Next, composition was defined as the area percent of each tissue type in each sample. Variation in tissue composition in the 2D-WSI cohort was defined as the distribution of composition of each tissue type segmented by the deep learning model. Variation in tissue composition in the 3D-CODA cohort was defined as the distribution of composition of each tissue type along the z-dimension of the serial stack of images, taking each serial histological image as an independent measurement. Minimum, maximum, mean, median, standard deviation, and histogram bin counts of each tissue component composition in the 2D-WSI and 3D-CODA cohorts were determined. In determination of the distribution of tissue composition in the 3D-CODA cohort, samples containing >90 serial images were randomly subsampled to contain 90 consecutive images.

Calculation of the number of tissue microarrays necessary to understand WSI and 3D tissue composition

Virtual TMAs (vTMAs) were generated in the 2D-WSI and 3D-CODA samples. First, a 2D or 3D coordinate was generated. Pixels were extracted corresponding to a 1 \times 1 mm² square surrounding the coordinates. A circular filter was applied to this extracted square to leave a 1-mm diameter disk representing a vTMA taken from the 2D or 3D image. To determine the number of vTMAs necessary to accurately estimate the tissue composition of a WSI or 3D pancreatic cancer tissue sample, random coordinates were determined, virtual TMAs were generated, and the tissue composition of each vTMA was recorded. Error was calculated between the per-class vTMA tissue composition and the overall composition of the WSI or 3D tissue sample. Another random vTMA was generated, added to the first vTMA, and error was recalculated for the combined sampling of two vTMAs. This process was repeated for sampling of up to 800 vTMAs on the 3D tissue samples and up to 100 vTMAs on 2D-WSIs. One thousand such simulations were performed to determine the general trend of per-class TMA error in assessment of WSI and 3D sample tissue composition.

Calculation of the decay in spatial correlation within 2D and 3D samples

In each sample of the 3D-CODA cohort, 2D planes of pixels were extracted from each classified tissue volume. For each segmented tissue component, the cross-correlation of the pixels classified as that component in that plane to all other planes of the 3D-sample was determined, and this correlation along with the distance between the planes was recorded. This process was repeated for all possible combinations of z-planes in a volume, and was repeated for each of the seven tissue samples. Aggregate correlation of



Cell Reports Methods Resource

composition of a single tissue component as a function of distance within a 3D sample was defined as the mean cross-correlation of that tissue component across all images of all samples.

Calculation of the change in tissue composition along vTMA cores

Change in tissue composition along serial sections of a vTMA core was determined. First, manual selection of coordinates on the first image of a sample was selected corresponding to a region visibly seen to contain invasive cancer. Next, a virtual core was extracted from the 3D segmented tissue volume corresponding to a cylinder of 3 mm diameter. Serial vTMAs were taken from each core, and the tissue composition of each serial vTMA was determined. Error in composition of each tissue type between the initial, manually selected vTMA and each serial TMA was calculated, and recorded along with the section number of that virtual serial TMA.

Calculation of the number of sections necessary to understand neoplastic content

Pancreatic neoplastic content was defined in two ways. For pancreatic cancer precursor lesions, PanIN content was defined as the volume of PanIN normalized by the combined volume of PanIN and normal ductal epithelium. For pancreatic cancer, PDAC content was defined as the volume of PDAC normalized by all PDAC, epithelial ducts, and PanIN total volume of the 3D sample. For each 3D sample, subvolumes were extracted corresponding to all combinations of between 1 and 90 serial tissue images. For each unique combination, the neoplastic content of the subvolume was calculated, and the relative error of this content was determined in relation to the neoplastic content of the whole 3D volume. For each 3D sample, measurements were grouped by the number of serial images contained in each subvolume.

QUANTIFICATION AND STATISTICAL ANALYSIS

All statistical analyses were performed using MATLAB scripts, with specific test employed as indicated. All significance tests were performed using the Wilcoxon rank-sum test. To compare metrics within and between cohorts, median, mean, standard deviation, and interquartile range were determined. Relative error was defined as [measured value – expected value]/expected value. No other statistical calculations were performed in this work.